# Radar Characteristics of Precipitation Features in the EPIC and TEPPS Regions of the East Pacific

R. CIFELLI, S. W. NESBITT, AND S. A. RUTLEDGE

*Colorado State University, Fort Collins, Colorado*

W. A. PETERSEN

*University of Alabama in Huntsville, Huntsville, Alabama*

S. YUTER

*North Carolina State University, Raleigh, North Carolina*

(Manuscript received 17 February 2006, in final form 29 June 2006)

ABSTRACT

Ship-based radar data are used to compare the structure of precipitation features in two regions of the east Pacific where recent field campaigns were conducted: the East Pacific Investigation of Climate Processes in the Coupled Ocean–Atmosphere System (EPIC-2001; 10°N, 95°W) in September 2001 and the Tropical Eastern Pacific Process Study (TEPPS; 8°N, 125°W) in August 1997. Corresponding July–September 1998–2004 Tropical Rainfall Measuring Mission (TRMM) precipitation radar (PR) data are also used to provide context for the field campaign data. An objective technique is developed to identify precipitation features in the ship and TRMM PR data and to develop statistics on horizontal and vertical structure and precipitation characteristics. Precipitation features were segregated into mesoscale convective system (MCS) and sub-MCS categories, based on a contiguous area threshold of 1000 km$^2$ (these features were required to have at least one convective pixel), as well as an "other" (NC) category. Comparison of the satellite and field campaign data showed that the two datasets were in good agreement for both regions with respect to MCS features. Specifically, both the satellite and ship radar data showed that approximately 80% of the rainfall volume in both regions was contributed by MCS features, similar to results from other observational datasets. EPIC and TEPPS MCSs had similar area distributions but EPIC MCSs tended to be more vertically developed and rain heavier than their TEPPS counterparts. In contrast to MCSs, smaller features (NCs and sub-MCSs) sampled by the ship radar in both regions showed important differences compared with the PR climatology. In the EPIC field campaign, a large number of small ($<$100 km$^2$), shallow (radar echo tops below the melting level) NCs and sub-MCSs were sampled. A persistent dry layer above 800 mb during undisturbed periods in EPIC may have been responsible for the high occurrence of these features. Also, during the TEPPS campaign, sub-MCSs were larger and deeper with respect to the TRMM climatology, which may have been due to the higher than average SSTs during 1997–98 when TEPPS was conducted. Despite these differences, it was found that for sizes greater than about 100 km$^2$, EPIC precipitation features had 30-dB$Z$ echos at higher altitudes and also had higher rain rates than similar sized TEPPS features. These results suggest that ice processes play a more important role in rainfall production in EPIC compared with TEPPS.

## 1. Introduction

Previous studies have shown the importance of precipitation processes in the tropical east Pacific region to the global circulation (Xie et al. 2005; Wang and Enfield 2001, 2003). This area, extending from the Central American coastline west to about 140°W and from the equator north to near 15°N, marks a transition region from a strong rising branch and heat source of the meridional Hadley circulation over the landmass and Gulf of Mexico to the descending branch of the zonal Walker circulation at the western extreme (Newell et al. 1974). The east Pacific is also one of the most im-

*Corresponding author address:* Robert Cifelli, Department of Atmospheric Science, Colorado State University, Fort Collins, CO 80523-1371.
E-mail: rob@atmos.colostate.edu

DOI: 10.1175/MWR3340.1

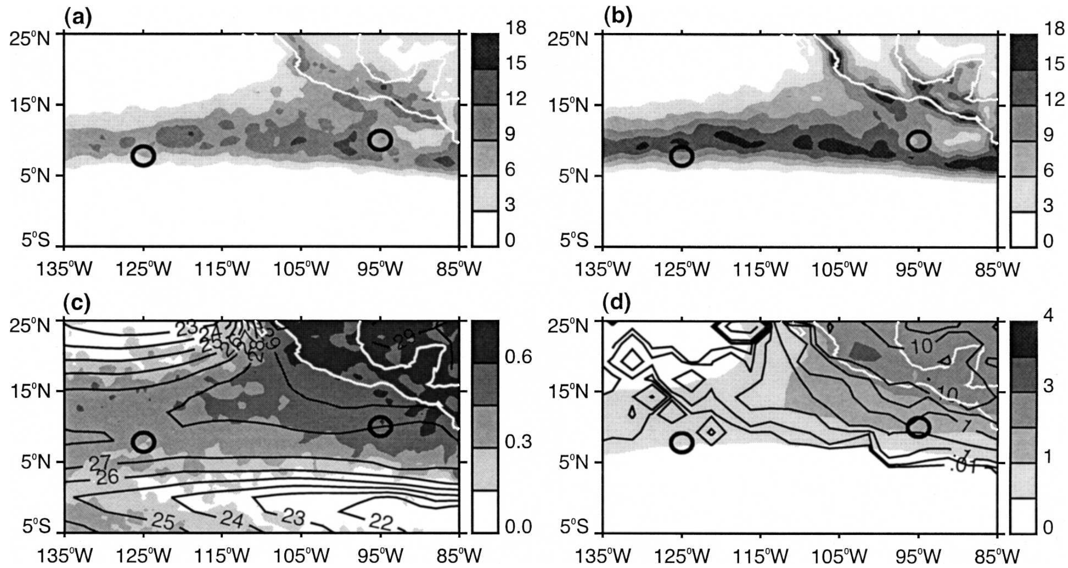


FIG. 1. August–October 1998–2004 (a) TRMM PR rainfall (mm day$^{-1}$), (b) TMI rainfall (mm day$^{-1}$), (c) PR convective fraction (shaded) and NCEP SST (contoured, °C), and (d) mean maximum precipitation feature height of 30-dB$Z$ echo (shaded, km) and lightning imaging sensor (LIS) lightning flash rate (contoured, flash day$^{-1}$ km$^{-2}$). The location of the EPIC and TEPPS field campaign regions are indicated with black circles in (a)–(d). The rainfall, convective fraction, and feature height data are derived from TRMM 3G68, version 6, products 2A25 and 2A12 for the PR and TMI, respectively.

portant genesis regions for tropical cyclones (Molinari et al. 2000).

Despite the importance of the region to global climate, recent studies have demonstrated that coupled ocean–atmosphere models do a poor job of representing the seasonal cycle of sea surface temperatures (SSTs) and atmospheric circulations in the region (Mechoso et al. 1995). Raymond et al. (2003) pointed out that the representation of deep convective processes in this area is a major source of uncertainty in coupled models. The East Pacific Investigation of Climate Processes in the Coupled Ocean–Atmosphere System (EPIC-2001) field campaign was conceived, in large part, to better understand long-term and subseasonal-scale variability in the east Pacific and to eventually improve model forecasts in the region (Raymond et al. 2004).

In addition to numerical model uncertainties, the east Pacific also represents a region of significant uncertainty in rainfall. In particular, recent satellite studies have highlighted large differences in rainfall gradients across the Pacific basin, including the east Pacific region, using different satellite algorithm retrievals based on IR brightness temperature and emission-based methods (Janowiak et al. 1995; Xie and Arkin 1996; Berg et al. 2002). Indeed, the Tropical Eastern Pacific Process Study (TEPPS) was carried out in large part to address the issue of rainfall discrepancies in the east Pacific (Yuter and Houze 2000). Comparison of selected ship radar, satellite IR, and satellite microwave data from TEPPS indicated that IR imagery and radar reliably detected rainy areas for large, long-lived features with IR brightness temperatures <235 K, but detection varied significantly for features of shorter duration and warmer brightness temperatures (Yuter and Houze 2000). Compared with IR, microwave retrievals generally produced better qualitative agreement with the ship radar over a wider range of precipitation feature sizes.

Berg et al. (2002) highlighted large differences in Tropical Rainfall Measuring Mission (TRMM) rainfall estimates in selected regions of the east and west Pacific between the precipitation radar (PR) and the TRMM microwave imager (TMI). The Berg et al. study pointed out differences in the effective rain layer thickness between the east and west Pacific and the potential effect on microwave retrieval algorithms. The discrepancies in the east Pacific are shown more clearly in Fig. 1. In both the EPIC (10°N, 95°W) and TEPPS (8°N, 125°W) regions, the TMI (Fig. 1b) overestimates with respect to the PR (Fig. 1a), with somewhat better agreement in the EPIC region compared with TEPPS. Because rainfall is directly coupled to integrated latent heating and its resulting impact on the large-scale circulation, it is important to understand why satellite retrieval algorithms show large disagreements in this part of the Tropics.

A prime motivation for this study is to explore the differences in east Pacific ITCZ convection and precipitation processes using ship-based and spaceborne radar data collected in the EPIC and TEPPS regions. TRMM PR data are integrated into the analysis to provide a climatological context for the field campaign results. Because this study uses an objective approach to identify precipitation features and analyze their horizontal and vertical characteristics in both ship and PR data, the approach could be eventually extended to other geographical regions where field programs have been conducted. The paper is organized as follows: section 2 describes the techniques used to analyze the radar data and section 3 provides some discussion of the environmental conditions in the east Pacific both in terms of when the field programs were conducted and in terms of climatology. Section 3 also describes the radar results in terms of vertical and horizontal characteristics and precipitation, and it contrasts the results between the EPIC and TEPPS regions. Conclusions are presented in section 4.

## 2. Data and methodology

The datasets collected during the EPIC and TEPPS field programs are similar: both experiments were focused in their respective ITCZ locations for approximately 3 weeks (20 days in EPIC; 16 days for TEPPS), radar data were collected nearly continuously throughout each campaign using the 5-cm scanning Doppler radar onboard the National Oceanic and Atmospheric Administration research vessel *Ronald H. Brown* (*RHB*), and upper air soundings were launched at a frequency of 6 times per day.

In both EPIC and TEPPS, Vaisala RS80 sondes were launched and data recorded using Vaisala software and a Digicora sonde system. The sonde data were quality controlled (QCed) at the Joint Office for Science Support at the National Center for Atmospheric Research (NCAR) using methods similar to those used to quality control the Tropical Ocean Global Atmosphere (TOGA) Coupled Ocean–Atmosphere Response Experiment (COARE) sounding data (Loehrer et al. 1996). Convective available potential energy (CAPE) was calculated assuming a 50-mb mixed layer and pseudoadiabatic ascent with no contribution from ice processes.

Detailed descriptions of the radar data collected in TEPPS and EPIC field campaigns are provided in Yuter and Houze (2000) and Petersen et al. (2003), respectively. In this study, all available volume scan data from the *RHB* were utilized (10-min resolution in EPIC and approximately 6-min resolution in TEPPS). A +3.6-dB offset was added to the TEPPS *RHB* data, based on the best estimates of radar calibration bias. No correction was applied to the EPIC *RHB* data since calibration procedures and comparisons with the TRMM PR during overpasses indicated a bias less than 1–2 dB during the field program. A similar assessment of the stability of the EPIC *RHB* radar calibration was determined by Mapes and Lin (2005).

The radar data were QCed using an algorithm from the National Aeronautics and Space Administration (NASA) TRMM Office to remove spurious echoes (e.g., sea clutter, anomalous propagation, and second-trip echo). While the QC algorithm generally performed favorably, inspection of the radar data showed that the QC algorithm sometimes removed the low-level precipitation echo in addition to the spurious echo. However, the precipitation echoes were weak (mostly less than 10 d$BZ$) and did not adversely impact the data processing and resulting echo statistics. An attenuation correction procedure following Patterson et al. (1979) was applied to both the EPIC and TEPPS *RHB* datasets in order to account for signal loss in heavy precipitation and correct C-band radar reflectivity. The radar data were then interpolated to a Cartesian grid using the NCAR REORDER software (Mohr et al. 1986) extending 110 km in $x$ and $y$ from a fixed point (7.8°N, 125°W for TEPPS and 10°N, 95°W for EPIC) in the horizontal direction at 3-km vertical and horizontal resolution.

The choice of grid resolution and maximum range were made to reflect the fact that between the TEPPS and EPIC campaigns, the *RHB* C-band radar was upgraded and the 3-dB beamwidth of the antenna was decreased from 1.54° to 0.95°. Thus, the spatial resolution of the radar data was improved significantly after TEPPS and prior to the EPIC field campaign. To objectively compare radar echo features from the two datasets with different spatial resolution, the data were interpolated to a Cartesian grid such that the gridded resolution did not exceed the actual spatial resolution of either dataset at maximum range. Thus, the maximum range was set as a compromise between obtaining as many echoes as possible and a resolution that allowed for the reasonable identification of vertical and horizontal structure.

Version 6 of the TRMM PR data was also incorporated into this study. The PR data are from 1998 to 2004 and are analyzed similar to Nesbitt et al. (2006) using the volumetric radar reflectivity product 2A25 (Kum-

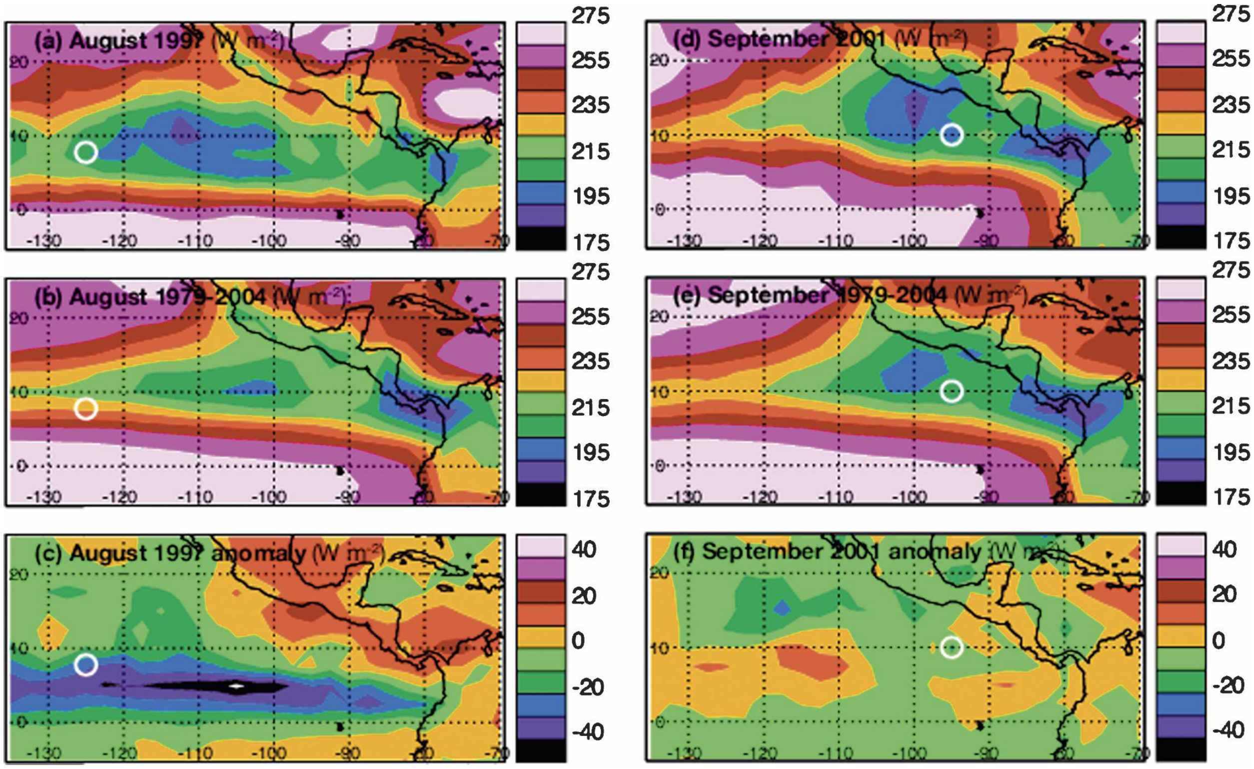


FIG. 2. East Pacific monthly OLR (a) composite for August 1997, (b) 1979–2001 August climatology, and (c) difference between August 1997 and the August 1979–2001 climatology. (d)–(f) Same as (a)–(c)but for September 2001. White circles in (a)–(c) indicate the location of the TEPPS field experiment while the circles in (d)–(f) indicate the location of the EPIC campaign.

merow et al. 1998). The PR data are analyzed for the months of July–September over a 5° × 5° region centered on the nominal campaign-specified ship radar location for both EPIC and TEPPS. Because of the 1997/98 El Niño, the ITCZ in the east central Pacific was shifted south of its normal position during the TEPPS campaign (Yuter and Houze 2000; see also Fig. 2). Sensitivity tests were therefore performed to examine the impact of the selected domain region on the resulting PR statistics in the TEPPS region. The meridional extent of the TEPPS domain was increased to 10° (i.e., the north–south endpoints were expanded from 5° to 15°N) in order to better capture the entire ITCZ region near 125°W. Enlarging the domain size increased the sample size but had minimal impact on the statistical properties of precipitation features (defined below); however, the tests did increase confidence that the results of this study are applicable to the entire ITCZ region of the east central Pacific.

The reflectivity profiles in the TRMM 2A25 rainfall product have been corrected for attenuation using a hybrid of the Hitschfeld–Bordan and the surface reference technique (Iguchi and Meneghini 1994; Iguchi et al. 2000); the latter is also used to retrieve the drop size distribution (DSD) in the profile. In this study, rain rates are calculated using the same $Z$–$R$ relationship as in the *RHB* dataset (described below), as opposed to the 2A25 rainfall product. This allowed for more meaningful comparisons between the ship and satellite datasets. Because of a increase in the satellite orbit, the TRMM data have an effective pixel resolution of 4.2 km prior to August 2001 and 4.5 km thereafter. These data are interpolated to a 3-km spacing in the vertical, similar to the *RHB* data. Following Nesbitt et al. (2006), features (1 pixel or larger in size) in the TRMM PR dataset are filtered to remove echoes less than 20 dB$Z$ to avoid noise contamination. Radar echo-top heights are also calculated using a 20-dB$Z$ minimum value. Although the horizontal resolution and minimum sensitivity of the TRMM PR and *RHB* datasets are different, the results, as described below, are consistent in a statistical sense and suggest that they can be used to provide meaningful comparisons.

Precipitation features were identified in both the ship and PR interpolated radar data using an objective algorithm to isolate contiguous regions of echo at the lowest grid level (1.5-km AGL) with radar reflectivity greater than or equal to 10 dB$Z$ in the ship data and 20 dB$Z$ in the PR data.[1] Similar to criteria used in TRMM satellite products (Nesbitt et al. 2000), sides or corners of diagonally adjacent pixels meeting the reflectivity criteria are considered to be part of the same feature. For each identified feature, the statistics of rainfall rate at 1.5-km altitude, number of grid elements, and vertical structure (maximum height of selected radar reflectivity thresholds) were retained.

To examine the distribution of precipitation features in more detail and to facilitate comparisons with previous studies, grid elements within each feature were classified as convective versus stratiform using the Steiner et al. (1995) partitioning algorithm. Identified features were further classified as mesoscale convective systems (MCSs) or sub-MCSs based on their continuous areal coverage and the existence of convective pixels. Features occupying $\geq$1000 km$^2$ and containing at least one convective grid element were considered to be MCSs while features containing at least one convective grid element but smaller than 1000 km$^2$ were considered sub-MCSs. The requirement of at least one convective element was employed so that maximum echo heights could be correlated to convective elements and related to previous studies of oceanic convection (e.g., Rickenbach and Rutledge 1998). The 1000-km$^2$ threshold was developed to be consistent with previous MCS radar echo definitions (Houze 1993). Features that did not meet the one convective element criterion were classified as other (NC), regardless of their size. Thus, four categories of features were examined: MCS, sub-MCS, NC, and total (MCS, sub-MCS, and NC combined).

To estimate precipitation feature rainfall for both TEPPS and EPIC, a power-based $Z$–$R$ relation of the form

$$Z = 218R^{1.6}, \tag{1}$$

is used, where $Z$ is the radar reflectivity (mm$^6$ m$^{-3}$) and $R$ is the rain rate (mm h$^{-1}$). The $Z$–$R$ was derived from Particle Measuring System (PMS) two-dimensional cloud and precipitation (2D-P) optical probe data collected by the NCAR C-130 research aircraft that flew a series of flight legs across the ITCZ region during the EPIC field experiment (D. Baumgardner 2002, personal communication). To derive the $Z$–$R$, all 2D-P data from flights within 1000 km of the *RHB* and heights at or below 1.5-km altitude were utilized.[2] Although Eq. (1) may not be representative of the entire spatial scale of precipitation features sampled by the radar, it does provide a way to compare the rainfall characteristics in the EPIC and TEPPS regions. Moreover, for the purposes of this study, the choice of the $Z$–$R$ relation does not change the overall results.

## 3. Results

### a. Environmental characteristics

To provide a context for the ensuing radar statistics, it is useful to describe the large-scale environmental conditions of the EPIC and TEPPS regions. Figure 2 shows the monthly outgoing longwave radiation (OLR) signature across the Pacific for the specific month and year of each field program as well as the 1979–2001 climatology for the region. Because OLR is related to cloud-top brightness temperatures, the index is often used as a crude proxy for convective activity.

Figures 2a–c show OLR brightness temperatures across the east Pacific for the month of August when the TEPPS campaign was conducted. The OLR data shows that during August 1997 (Fig. 2a), the pattern of convection was quite different from the 23-yr climatology with large depressions in brightness temperature (presumably related to the more frequent occurrence of deep convection throughout the east Pacific). This pattern coincides with the 1997/98 El Niño (Yuter and Houze 2000). In the vicinity of the TEPPS region, OLR brightness temperatures were depressed in excess of ~30 K during August 1997 compared with climatology (Figs. 2b,c). However, despite the occurrence of an El Niño, the brightness temperatures sampled over the TEPPS domain during August 1997 were not as cold as temperatures sampled in September 2001 over the EPIC domain (cf. Figs. 2a,d).

Considering the east Pacific climatology for the month of September when EPIC was conducted, the OLR map shows two brightness temperature minima northwest and southeast of the EPIC domain (Fig. 2d). The former is associated with the preferred east Pacific tropical cyclone track (Vincent and Fink 2001) while the latter is associated with nearly ubiquitous rainfall observed in the region of the Panama Bight and western Columbia (e.g., Mapes et al. 2003). Brightness tem-

[1] Sensitivity tests were performed using both 10- and 20-dB$Z$ thresholds in the *RHB* data. Although increasing the threshold changes the magnitude of the *RHB* feature statistics, the relative trends are unaffected for all parameters with the exception of area and rain rate, which are described in detail in sections 3b and 3d, respectively.

[2] The $Z$–$R$ relation used herein is slightly different than the relation used in Raymond et al. (2003). Although both studies used data from the C-130 aircraft during EPIC-2001, the current study restricted data to within 1000 km of the *RHB* and included all data collected at or below 1.5-km AGL.

peratures are higher in the western portion of the domain, indicating generally shallower cloud systems on average. The September climatological OLR pattern (Fig. 2e) is consistent with echo-top distributions observed in the TRMM data (Fig. 1c). Although there is some suggestion that the convective intensity across the EPIC domain in 2001 was slightly more intense compared with climatology (Figs. 2d,f), the spatial distribution of OLR during September 2001 is largely consistent with the 1979–2001 climatology, suggesting that conditions during the EPIC campaign were not significantly different from normal.

With regard to SSTs, Fig. 1 shows that the TEPPS region is situated close to the equatorial cold tongue, near a large gradient in SSTs. In contrast, the EPIC region is somewhat removed from the cold tongue, being farther north and well within the east Pacific warm pool. SSTs are slightly warmer (<1°C) on average in the EPIC region compared with TEPPS, though they were similar during the respective field campaigns (29°C; not shown). Note that SSTs south of the EPIC region were colder than normal during the EPIC campaign (Zuidema et al. 2006), which may have had an influence on the resulting shallow cloud population that was sampled during the EPIC campaign as described below.

Figure 3 shows skew *T*–log*p* diagrams from the radiosonde data collected during the EPIC and TEPPS field experiments. Figure 3a shows a composite profile for each region using all available sonde data. Figures 3b,c show composite profiles during periods when sub-MCS activity was greater than average (i.e., sub-MCS feature area was less than average and ship-based radar 5-dB*Z* echo-top heights were lower than average) and periods when MCS activity was larger than normal (i.e., MCS feature size was greater than average and 5-dB*Z* echo-top heights were deeper than average), respectively. When combining all possible sounding data (Fig. 3a), the EPIC composite shows more moisture compared with TEPPS both at low levels (below about 800 mb) and above 450 mb, but is somewhat drier at midlevels. This midlevel dry layer is enhanced during undisturbed periods (Fig. 3c), consistent with documented midlevel dry intrusions over the far eastern Pacific during the EPIC campaign (Zuidema et al. 2006). As described below, the relative location of moister low-level air and drier midlevel air in the EPIC soundings compared with TEPPS had a significant impact on the resulting echo-top characteristics in the two regions. During disturbed periods (Fig. 3b), the midlevel dry layer disappears and both the EPIC and TEPPS composite soundings reflect conditions more conducive to deep convection. CAPE values are highest during the sub-MCS periods in both datasets with EPIC CAPE values being nearly a factor of 2 larger than TEPPS in all the composites (Table 1).

### b. *Feature horizontal and vertical structure characteristics*

A summary of ship and PR-sampled precipitation features identified in EPIC and TEPPS is provided in Table 2. The ship radar during the field campaigns (hereafter referred to as *RHB*) sampled nearly 100 000 features during EPIC and about 41 000 in TEPPS. The larger number of features observed during EPIC is at least partially due to the longer duration of the field program (20 versus 16 days), though the 25% increase in EPIC field campaign duration relative to TEPPS does not explain a 140% increase in the observed feature numbers. In both field programs, sub-MCSs were the dominant feature type, composing over 50% of the TEPPS dataset and nearly two-thirds of the EPIC *RHB* sample. The NC features were also commonly observed in both field programs but, as shown below, contributed little to the total rainfall. MCS features compose only a small portion (≤5%) of the observed feature numbers; however, as discussed below, these large features contributed the vast majority of the rainfall in both the EPIC and TEPPS regions. The 7-yr TRMM PR dataset catalogued fewer features over the EPIC and TEPPS regions; however, the relative fraction of feature types is similar to the *RHB* results, at least for the EPIC region. In the TEPPS region, there are somewhat more sub-MCSs and fewer NCs compared with the field campaign observations.

The distribution of feature sizes observed in the *RHB* and TRMM PR datasets is shown in Fig. 4 in terms of both cumulative probability and relative frequency. As expected, small features (<1000 km$^2$) in both the ship and satellite data dominate the radar echo population, producing a lognormal frequency of occurrence distribution (Fig. 4a). Similar distributions have been observed by radar in other oceanic regions [López (1977) and Houze and Cheng (1977) in the eastern Atlantic, Cetrone and Houze (2006) in the central Pacific, Nesbitt et al. (2006) in the global Tropics, and others). By definition, sub-MCSs fall into this category (Fig. 4c); however, Fig. 4d shows that the vast majority of NC features are also small. Examination of the *RHB* radar images showed that NCs sometimes occurred as decayed remnants from previous areas of active convection and sometimes occurred as isolated elements. Moreover, they were generally transient, rarely lasting more than 10–20 min in an image sequence, making it difficult to determine their origins and evolutionary characteristics. On average, NCs were the smallest

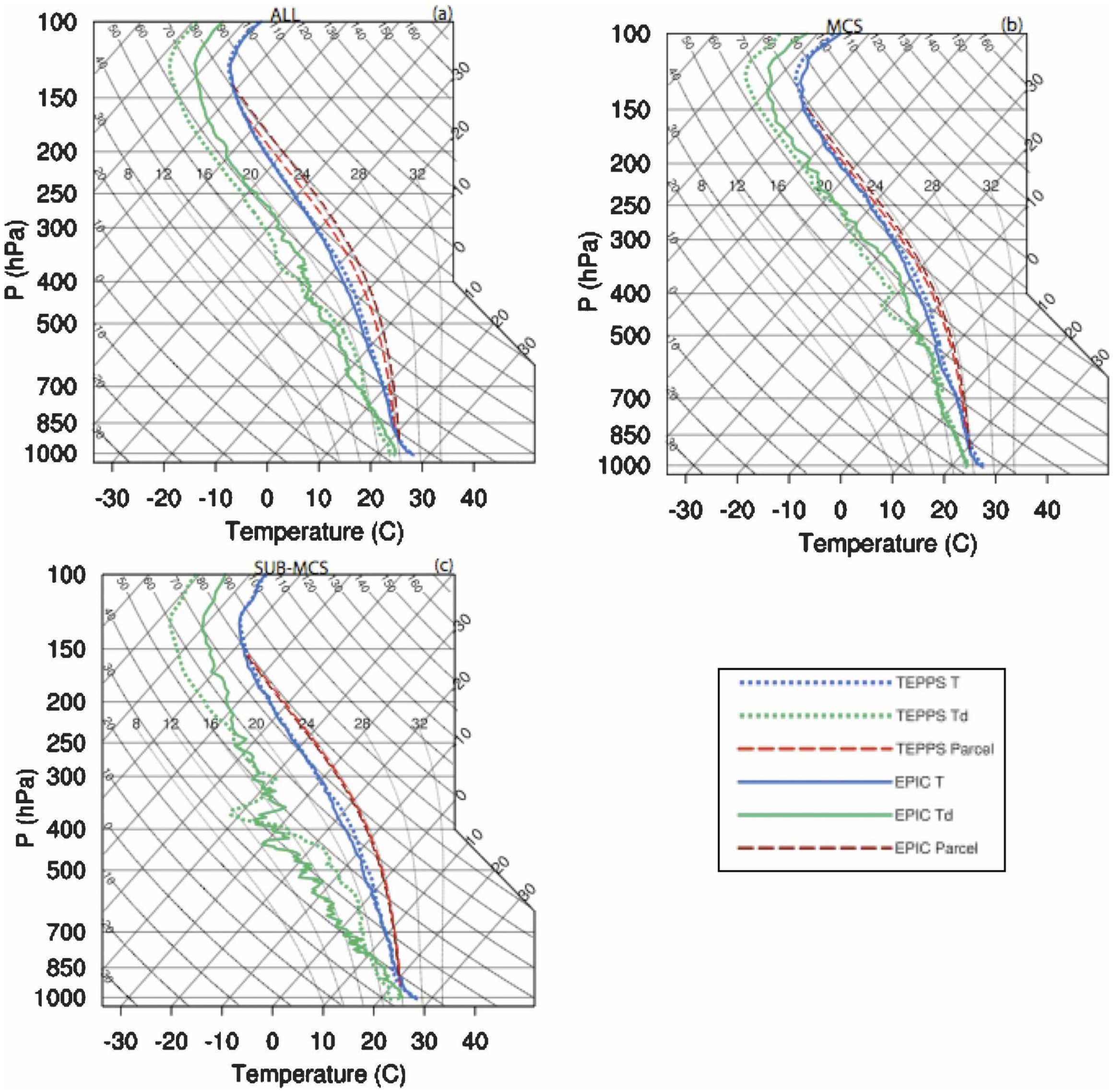


FIG. 3. Composite skew $T$–log$p$ diagrams for the EPIC and TEPPS campaigns for (a) all available radiosonde data, (b) MCS conditions, and (c) sub-MCS conditions. Solid (dashed) lines refer to EPIC (TEPPS) data with blue, green, and red lines representing temperature, dewpoint, and pseudoadiabatic ascent of a surface parcel, respectively.

feature type sampled by both the PR and ship radar (Table 2).

Considering all precipitation types together, the satellite climatology shows that the size distributions in the two regions are quite similar, with EPIC features being slightly larger in terms of mean (Table 2) or median (50% cumulative probability; Fig. 4a) characteristics. During the field campaigns, however, large differences in the feature size distributions are apparent. TEPPS *RHB* features are substantially larger compared with corresponding EPIC features. The larger average feature size in the TEPPS *RHB* data is due to a combination of larger sub-MCSs sampled during the TEPPS field campaign compared with the corresponding satellite climatology; hence, the TEPPS *RHB* size distribution is shifted to the right (larger area) of the TEPPS PR distribution in Fig. 4c. Also, there is an increased

TABLE 1. CAPE (J kg$^{-1}$) during the EPIC and TEPPS field programs. See text for definition of MCS and sub-MCS periods.

| | All periods | MCS periods | Sub-MCS periods |
|---|---|---|---|
| EPIC | 1833 | 1338 | 2408 |
| TEPPS | 903 | 716 | 1297 |

TABLE 2. Number of precipitation features observed in the EPIC 2001 and TEPPS 1997 *RHB* and 1998–2004 TRMM PR radar data. The numbers in prenthesis refer to the mean values of feature size in km$^2$.

| Dataset | Tot features | MCS features* | Sub-MCS features* | NC features |
|---|---|---|---|---|
| EPIC *RHB* | 93 071 (274) | 2779 (7108) | 57 519 (88) | 32 773 (22) |
| EPIC PR | 14 792 (351) | 591 (6275) | 9344 (124) | 4857 (68) |
| TEPPS *RHB* | 40 910 (433) | 1895 (5414) | 22 172 (163) | 16 843 (63) |
| TEPPS PR | 13 043 (312) | 456 (6396) | 8831 (100) | 3756 (76) |

* Feature contains at least one convective grid element.

occurrence of very small NCs sampled during the EPIC field campaign compared with the EPIC climatology, such that the EPIC *RHB* distribution is shifted to the left (smaller area) compared with the EPIC PR in Fig. 4d. The larger size of TEPPS sub-MCSs (70% increase over climatology) sampled in the *RHB* data is consistent with warmer SSTs during the El Niño conditions across the east Pacific in 1997. Because sub-MCSs tend to be prevalent when large-scale forcing is minimized (e.g., Sui et al. 1997; Rickenbach and Rutledge 1998), warmer SSTs might be expected to have a greater influence on the size of these features through increased

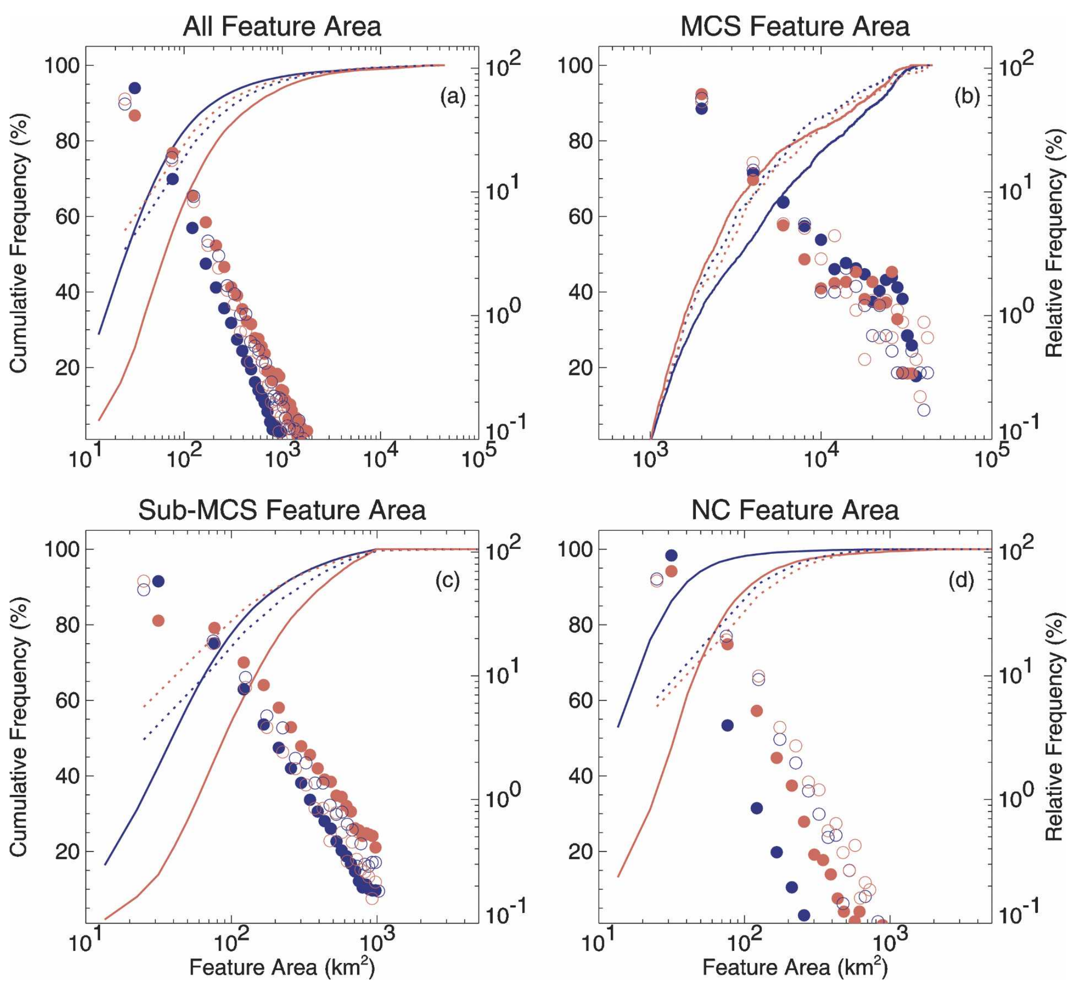


FIG. 4. Probability distributions of precipitation feature area (km$^2$) identified in EPIC and TEPPS radar data for (a) total feature, (b) MCS feature, (c) sub-MCS, and (d) NC category. Cumulative frequencies (left ordinate) are indicated by blue (red) lines for the EPIC (TEPPS) region. Solid (dashed) lines refer to *RHB* (TRMM PR) radar data. Probability distributions (right ordinate) are indicated by blue (red) circles for the EPIC (TEPPS) regions. Filled (open) circles refer to *RHB* (TRMM PR) radar data. Note the scale change of the abscissa in (a)–(d).

boundary layer fluxes. The increase in small NCs during the EPIC campaign is more difficult to explain but may be related to the periodic dry intrusions during the EPIC campaign. Figure 4d shows that there is little change in the NC size distribution during TEPPS compared with climatology.

Note that increasing the *RHB* feature threshold from 10 to 20 dB*Z* decreases the average feature size. This effect is especially pronounced for TEPPS NCs, which decrease in mean area by 57%, compared with the 10 dB*Z* threshold value shown in Table 2. Although the mean area changes, the relative differences between TEPPS and EPIC *RHB* features are preserved at either threshold.

In contrast to the smaller features, the MCS distributions sampled by the *RHB* during the EPIC and TEPPS field campaigns are similar to the PR climatologies for the two regions (Fig. 4b). The average area of the *RHB* MCSs is within 20% of their respective climatological mean values (Table 2). Apparently, changes in the ITCZ during the 1997/98 El Niño did not have as big an impact on the MCS distribution compared with the sub-MCSs. This may be becasue MCSs are expected to be prevalent when large-scale forcing has a significant influence on precipitation coverage and organization [e.g., easterly waves (Petersen et al. 2003) or tropical cycle activity] and probably outweigh effects due to changes in SST.

To explore differences in the vertical structure of features in the EPIC and TEPPS regions, both the mean maximum echo-top height distribution and reflectivity distributions at individual heights were analyzed. These parameters provide different measures of vertical structure; the former is associated with the total depth of features and can therefore be related to other proxies of convection that rely on cloud-top characteristics (e.g., IR brightness temperature).[3] The latter quantity is useful for evaluating the intensity of precipitation features and can provide information about the relative abundance of liquid and ice hydrometeors (in a statistical sense) within the different feature types.

The echo-top height distribution is shown in Fig. 5 and mean values are presented in Table 3 for the 20-dB*Z* threshold. Examining the TRMM satellite climatology of the two regions, Fig. 5 and Table 3 show that all categories of EPIC features are deeper compared with TEPPS. These differences are consistent with National Meteorological Center kinematic analyses presented in Janowiak et al. (1995): the EPIC region shows enhanced low-level convergence relative to TEPPS, which is most likely due to a combination of the TEPPS region being in closer proximity to the descending branch of the Walker circulation and EPIC's closer proximity to enhanced rising motion over the South and Central America region (Newell et al. 1974) as well as warmer SSTs. The difference in mean heights is reflected in the echo height distributions of Fig. 5: above 4.5 km, the 20-dB*Z* echo height distributions are shifted to the right (toward greater depths) in the EPIC PR data compared with TEPPS. The difference is especially pronounced in the sub-MCS category (Fig. 5c), and to a lesser extent, in MCSs and NCs deeper than about 10 km (Figs. 5b,d). Only at the lowest height bin (1.5 km) do TEPPS echo tops occur more often compared with EPIC in the PR dataset. The mean feature heights shown in Table 3 (total feature category) are consistent with previous studies of storm heights across the global Tropics (Short and Nakamura 2000); however, the TRMM PR data used in this study lacks the well-defined double peak structure observed by Short and Nakamura (2000). This is probably due to the coarse spatial resolution used in this study.

During the field campaigns, the echo height distributions show some important differences compared with the PR climatology, especially in the sub-MCS and NC categories. In particular, sub-MCS echo-top heights in the EPIC field campaign dataset are 27% smaller compared with the corresponding PR average while TEPPS echo-top heights are 50% larger (Table 3). In these categories, EPIC *RHB* echo tops were much more common compared with TEPPS at 1.5 km (i.e., trade wind cumulus level), while TEPPS *RHB* echo tops were more common between 4.5 and 7.5 km (i.e., likely cumulus congestus). The features with echo tops at 1.5 km correspond to sizes less than 100 km$^2$ (shown below). As described in previous studies, shallow clouds play an important role in moistening the boundary layer, preconditioning the atmosphere for deep convection (Johnson et al. 1999). The difference in EPIC and TEPPS *RHB* echo-top distributions is likely related to the more moist TEPPS environment above 800 mb during undisturbed periods when sub-MCSs were prevalent (Fig. 3c). All other factors being equal, the TEPPS environment during these periods would be conducive to the reduced entrainment of dry air and higher resulting echo tops compared with EPIC. The NCs sampled during both field campaigns were smaller than the climatological values. Because of the transient na-

[3] Because cloud-top cirrus likely have radar reflectivities below the detection limit of C-band radar, the satellite-measured cloud top and radar echo top will be different. Therefore, caution must be exercised in comparing (in a quantitative sense) IR brightness temperatures with mean maximum echo-top heights (e.g., Cifelli et al. 1996).

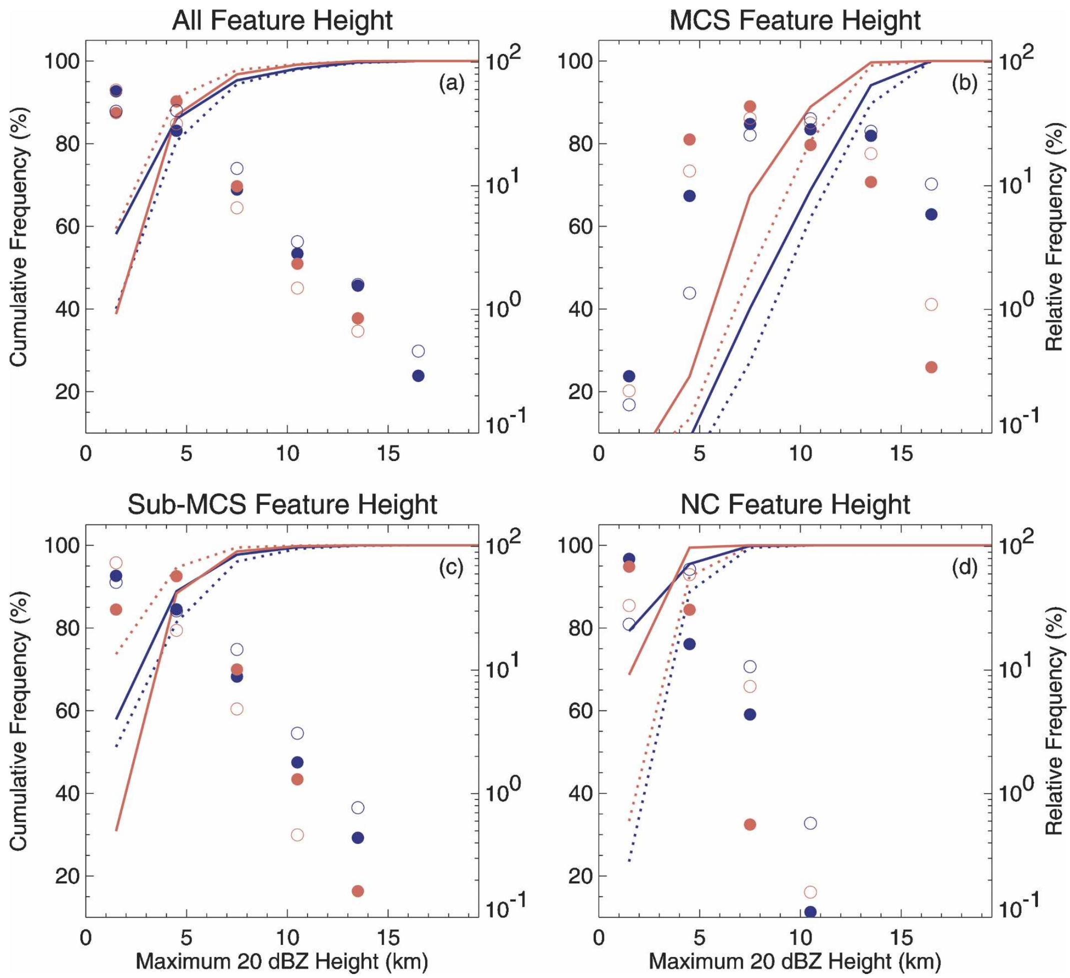


FIG. 5. Same as Fig. 4 but for mean maximum 20-dB$Z$ height (km).

ture of these features, it is difficult to interpret the changes relative to the PR climatology.

In contrast to the relatively small features (i.e., sub-MCSs and NCs), the MCS echo tops sampled during the field campaigns were similar (i.e., within 11%) to the PR climatologies for the two regions. Similar to the size distribution results described above, it appears that the El Niño conditions during August 1997 had little effect on the depth of large features in these two regions of the east Pacific and that the vertical development of these features is more likely to be influenced by large-scale disturbances. A recent study by Petersen et al. (2003) showed that during the EPIC campaign, a series of easterly waves traversed across the region. Deep convection with widespread echo coverage was especially pronounced during and immediately following the trough passage of these waves. Easterly waves were also documented in the TEPPS campaign; however, their vertical structure was more complicated (Serra and Houze 2002) and the accompanying effects on precipitation were apparently less pronounced than the waves crossing the EPIC region. The proximity of the EPIC region to the preferred tropical cyclone track in the east Pacific also provides conditions conducive to deep convection, so it is not surprising that MCS-scale precipitation is deeper than in the TEPPS region. These results are consistent with the IR brightness temperature climatology shown in Fig. 2.

To explore the relationship between feature size and vertical structure in more detail, the mean maximum echo-top height was analyzed as a function of feature

TABLE 3. Mean maximum 20-dB$Z$ echo-top heights (km) for the *RHB* and TRMM PR datasets.

| | All | MCS | Sub-MCS | NC |
|---|---|---|---|---|
| EPIC *RHB* | 2.1 | 10.1 | 2.7 | 0.6 |
| EPIC PR | 4.1 | 10.9 | 3.7 | 4.1 |
| TEPPS *RHB* | 3.3 | 8.1 | 3.9 | 1.5 |
| TEPPS PR | 3.1 | 9.1 | 2.6 | 3.7 |

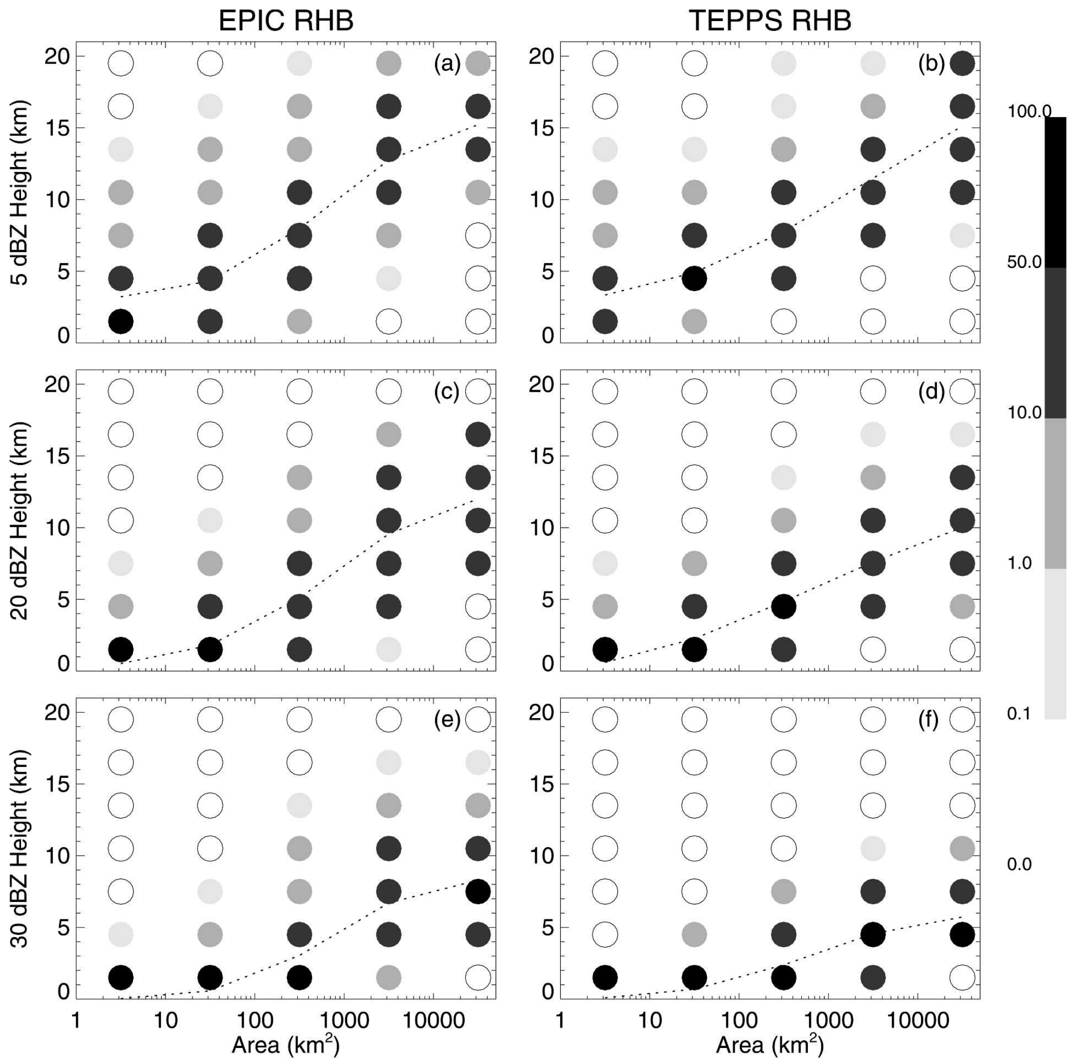


FIG. 6. *RHB* mean maximum echo-top height defined by (a), (b) 5-, (c), (d) 20-, and (e), (f) 30-dB*Z* threshold as a function of feature area. EPIC (TEPPS) *RHB* data are shown in (a), (c), (e) [(b), (d), (f)]. Relative frequency (%) of echo-top height occurrence is indicated by the circle shading, according to the legend at the rhs of the figure. The dotted line in (a)–(e) represents the mean of the distribution.

area for selected echo-top thresholds (Figs. 6, 7). The 5-, 20-, and 30-dB*Z* echo-top thresholds for the *RHB* data are shown in Fig. 6 while only the 20- and 30-dB*Z* echo-top thresholds are shown in Fig. 7 for the TRMM PR data, because the 5-dB*Z* echo-top threshold is below the sensitivity of the PR. As expected, the height of the echo top increases with feature area in both the *RHB* and PR datasets, which simply shows that large features tend to be deeper than smaller features. The satellite data (Fig. 7) show that EPIC features are generally deeper than corresponding TEPPS features for a given size bin. This is also true for the *RHB* data, especially at the higher echo-top thresholds (Figs. 6c–f) and for sizes above an area of several hundred square kilometers. However, below this area threshold, TEPPS *RHB* features are slightly deeper compared with EPIC. This small size range is composed of both sub-MCSs and NCs (Fig. 4). The reversal in the TEPPS–EPIC echo-top height pattern at the smallest size interval may be related to the persistent dry layer above 700 mb in the EPIC soundings during periods when sub-MCSs and NCs are prevalent (Fig. 3). Features with the smallest area would be expected to be the most susceptible to the entrainment of dry air and the resulting decrease in buoyancy. At 30 dB*Z* (Figs. 6e,f, 7c,d), the separation between EPIC and TEPPS becomes more distinct across the feature area spectrum. Because the height of the 30-dB*Z* echo above the freez-

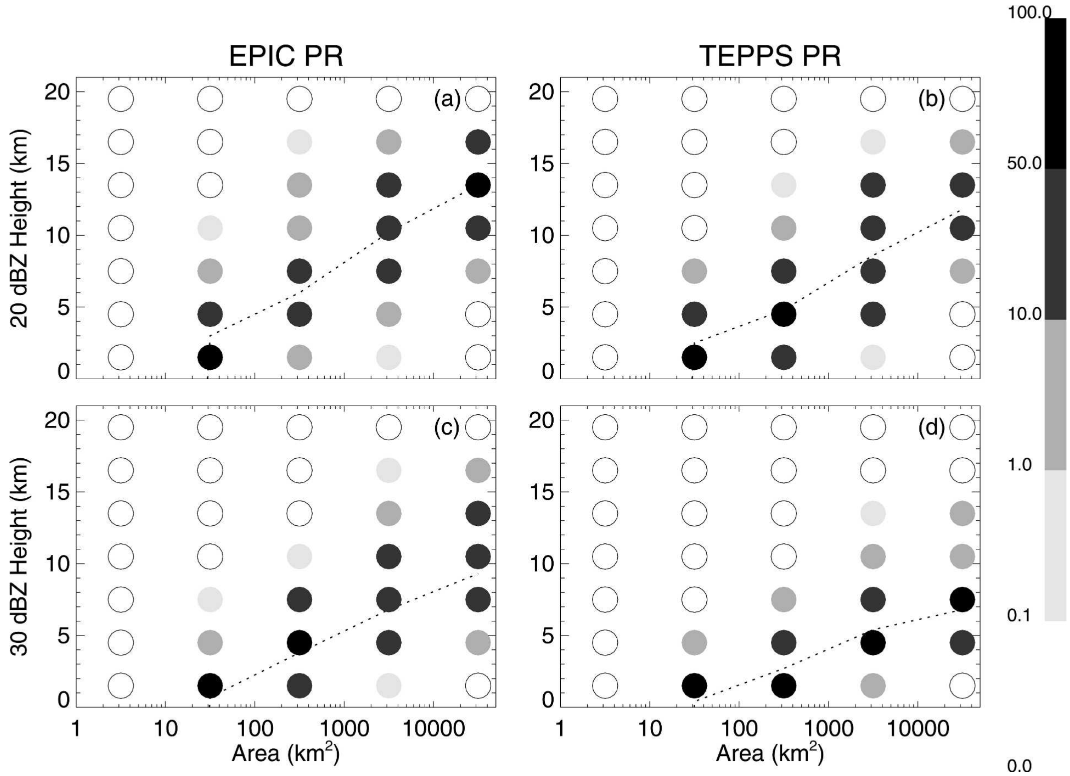


FIG. 7. Same as Fig. 6 but for the TRMM PR dataset.

ing level is often used as a proxy for the presence of graupel and resulting vertical intensity of convection (e.g., DeMott and Rutledge 1998), these plots suggest that EPIC features tend to have more vigorous vertical drafts and resulting mixed phase microphysical processes compared with TEPPS. As discussed below, this result may have important implications for rainfall production in the two regions.

### c. Convective and stratiform characteristics

In this section, characteristics of sub-MCS and MCS features are examined in more detail using the convective-stratiform partitioning algorithm described in section 2. Figure 8 shows the convective fraction of sub-MCS and MCS features for the *RHB* and PR datasets in the EPIC and TEPPS regions. MCSs provide the bulk of the convective rain volume contribution in both regions. In the field campaigns, the convective rain volume fraction is larger compared with the PR satellite climatology, especially in the TEPPS region. Although the differences are consistent with the higher spatial resolution of field campaign data (allowing better resolution of convective cells), anomalous SSTs during the 1997 El Niño may also be partially responsible for the differences in the TEPPS region. The difference is especially pronounced in the TEPPS region. Overall, the convective rainfall fraction in the EPIC region is larger compared with TEPPS, ranging from 46%–64% in EPIC to 29%–55% in TEPPS. The EPIC convective fractions are in agreement with similar radar results from the east Atlantic (Cheng and Houze 1979) and west Pacific during disturbed periods of TOGA COARE (Short et al. 1997). In terms of area fraction, there is little difference between the PR and *RHB* datasets for both regions: convective features account for about 24% of the total feature population in EPIC and 16%–18% in the TEPPS region.

A more detailed comparison of partitioned vertical structure for EPIC and TEPPS *RHB* precipitation features is shown in Figs. 9 and 10. These figures show vertical characteristics in both the convective and stratiform regions of sub-MCS (Fig. 9) and MCS features (Fig. 10) for the *RHB* dataset. The vertical characteristics are represented by contoured frequency by altitude diagrams (CFADs; Yuter and Houze 1995).

In the convective region (Figs. 9a,b, 10a,b), the CFADs of both the MCS and sub-MCS categories have the anticipated pattern of the more probable occurrence of intense reflectivities (i.e., wide CFAD) at low levels and the reduced probability of high reflectivities as height increases (i.e., CFAD narrows with height). Although similar at low levels, important differences

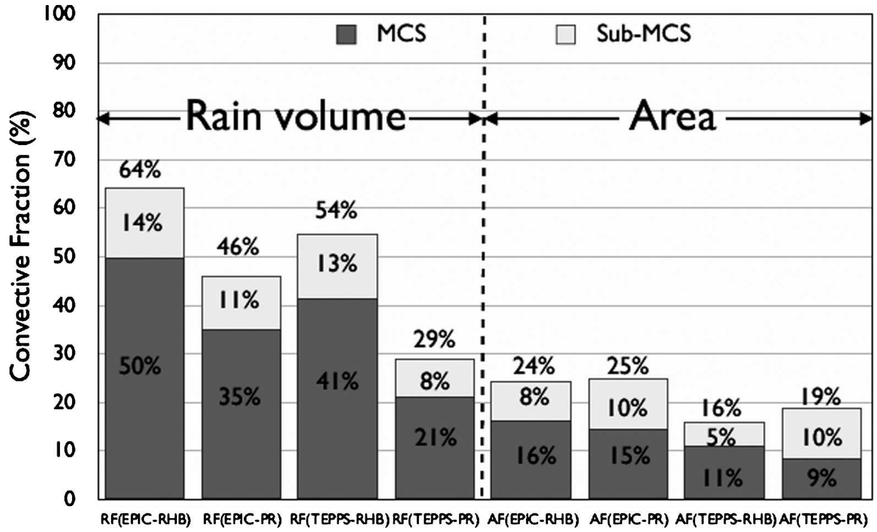


FIG. 8. Convective fraction for MCSs (dark shading) and sub-MCSs (light shading) in the EPIC and TEPPS regions. The four bar graphs on the left and right represent rain volume convective fraction (RF) and rain area convective fraction (AF), respectively. The number above each bar graph indicates the total convective fraction.

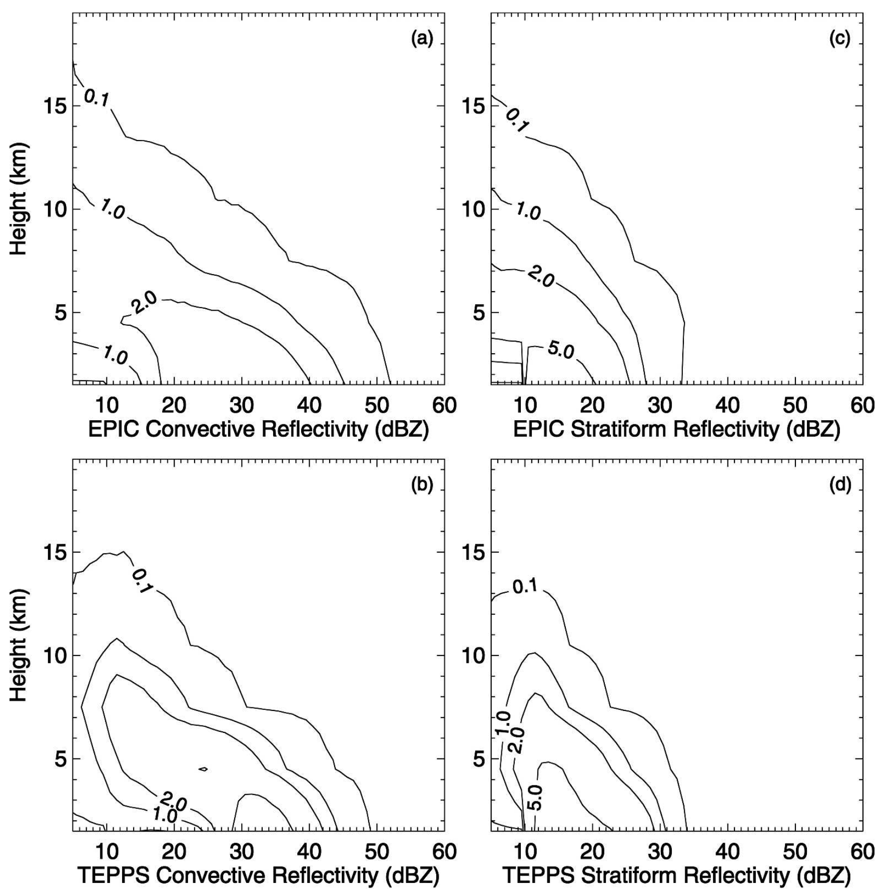


FIG. 9. CFAD distributions of *RHB* radar reflectivity (dB$Z$) for sub-MCS features in (a), (c) EPIC and (b), (d) TEPPS. Convective (stratiform) distributions are shown in (a), (b) [(c), (d)] columns. The reflectivity bin size is 1 dB. Contours indicate the relative frequency of occurrence (%) at each vertical level.

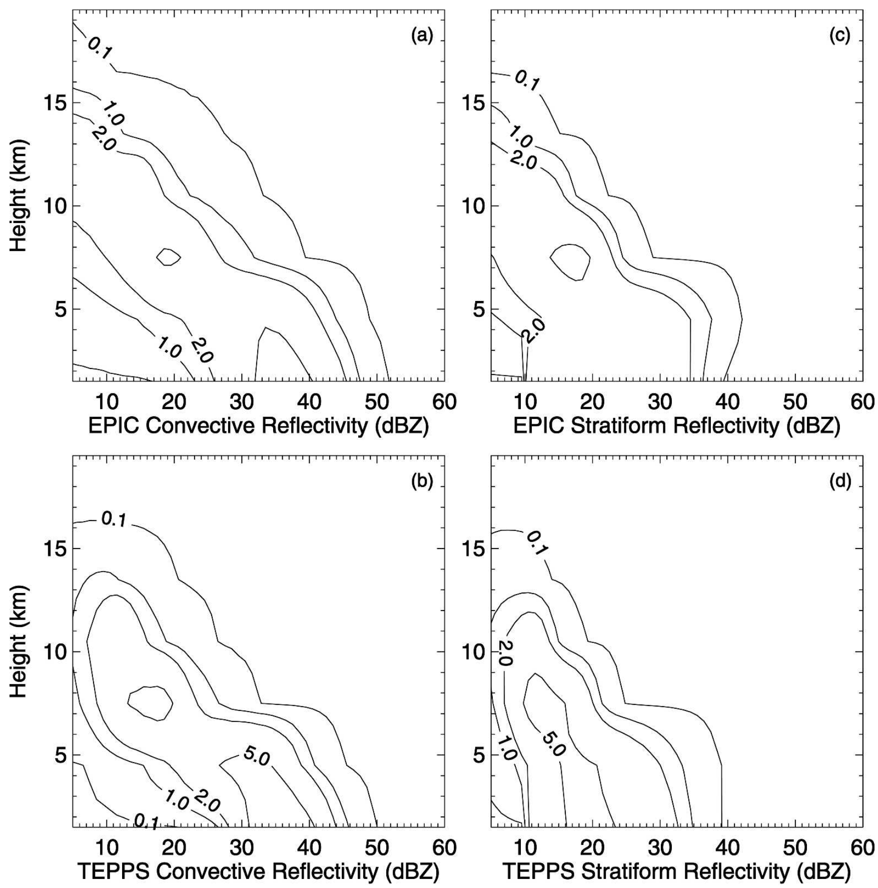


FIG. 10. Same as Fig. 9 but for the MCS feature category.

between the EPIC and TEPPS distributions occur above the melting level (near 5 km) in both the convective sub-MCS and MCS distributions. The EPIC convective CFADs are wider, with the tail of the reflectivity distribution (e.g., 30 dB$Z$) extending to higher heights compared with TEPPS. This indicates the existence of more precipitation-sized ice and the more likely occurrence of graupel in EPIC convection, consistent with the lightning frequency map shown in Fig. 1. Thus, although both EPIC and TEPPS convective features can be deep (as shown in Figs. 9 and 10 by the 0.1% probability contour extending above 15 km), the CFADs suggest important differences in the distribution of ice above the freezing level in the two regions.

As expected, the MCS distributions extend to greater altitudes compared with sub-MCSs. MCSs would be expected to be longer lived than sub-MCSs and develop more pronounced internal circulations with larger updrafts that are less susceptible to entrainment mixing and more efficient in the processing of available CAPE. Moreover, because of their larger size, MCSs are less susceptible to beam filling sampling issues. It follows that MCSs would generally have more vigorous convection, as reflected in the increased occurrence of 30 dB$Z$ above the melting level, compared with sub-MCSs. This can be seen by comparing the height of given frequency thresholds in Figs. 9 and 10.

In the stratiform region, the MCS distributions (Figs. 10c,d) show a reflectivity enhancement near the melting level associated with the radar bright band. This feature is more pronounced in EPIC (Fig. 10c) compared with TEPPS (Fig. 10d). Both the EPIC and TEPPS stratiform distributions show a rapid falloff with height above the melting level. The modes of the MCS stratiform distributions are higher compared with the sub-MCSs in both the EPIC and TEPPS regions (cf. Figs. 9c,d, 10c,d). Similar to the convective distributions, the EPIC stratiform CFADs are noticeably wider above the melting level than their TEPPS counterparts for both the sub-MCS and MCS categories and presumably reflect differences in ice content distribution above the freezing level (Petersen et al. 2005). These differences in vertical structure and, by inference, ice water path have important implications for the microwave

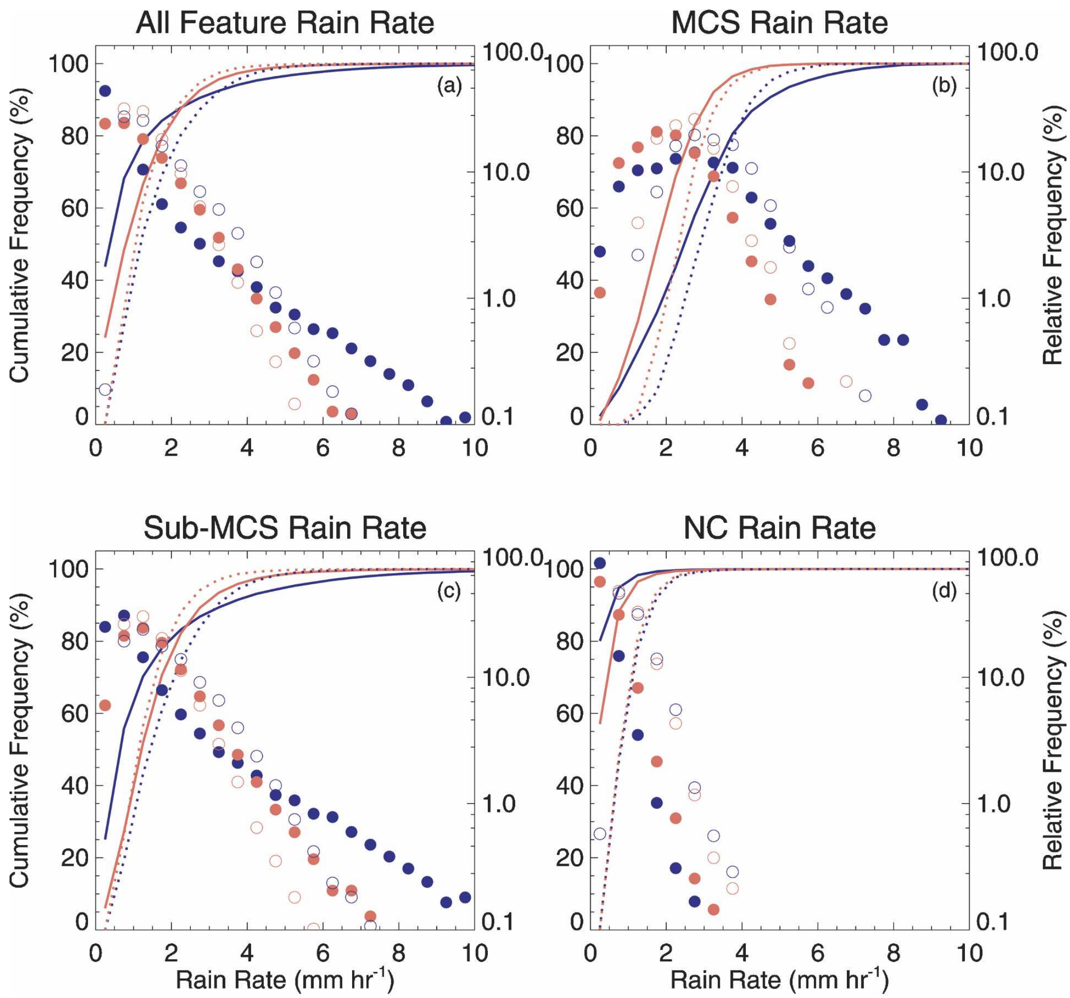


FIG. 11. Conditional rain-rate distributions for the (a) all, (b) MCS, (c) sub-MCS, and (d) NC feature categories. Cumulative frequencies (left ordinate) are indicated by blue (red) lines for the EPIC (TEPPS) region. Solid (dashed) lines refer to *RHB* (TRMM PR) radar data. Probability distributions (right ordinate) are indicated by blue (red) circles for the EPIC (TEPPS) regions. Filled (open) circles refer to *RHB* (TRMM PR) radar data.

scattering signature of features in these regions (DeMott and Rutledge 1998; Berg et al. 2002). Although not shown, the PR CFADs show similar trends to the *RHB* results in Figs. 9 and 10.

### *d. Precipitation characteristics*

In this section, rainfall characteristics of the EPIC and TEPPS features are explored and related to the vertical structure results in section 3b. Conditional rain-rate histograms and cumulative frequency diagrams for the different feature categories are shown in Fig. 11 and mean values are listed in Table 4. We begin by comparing the satellite climatologies for the respective regions and then discuss differences in the field campaign (*RHB*) results.

Because of the difference in sensitivity between the PR and *RHB* radar, caution must be exercised in comparing the field campaign and satellite datasets, especially at low rain rates. The minimum detectable rain rate in the TRMM PR data is about 0.6 mm $h^{-1}$ compared with 0.1 mm $h^{-1}$ in the *RHB* dataset.[4] The difference in sensitivity translates into a total rain volume of approximately 3%–6% that is missed by the TRMM PR (not shown). The result of the difference in rainfall sensitivity is to shift the TRMM PR cumulative and relative frequency distributions to the right of the corresponding *RHB* distributions in Fig. 11 and increase the mean rain rates (Table 4). However, the *RHB* distributions are wider than their PR counterparts (Fig.

[4] The minimum rain rates are calculated using a 20- (10) d$BZ$ threshold for the PR (*RHB*) and applying Eq. (1).

TABLE 4. Mean rain rate (mm h$^{-1}$) by feature category.

| | All | MCS | Sub-MCS | NC |
|---|---|---|---|---|
| EPIC *RHB* | 2.7 | 2.9 | 2.3 | 0.4 |
| EPIC PR | 3.2 | 3.6 | 2.5 | 1.3 |
| TEPPS *RHB* | 2.0 | 2.2 | 1.8 | 0.5 |
| TEPPS PR | 2.7 | 3.1 | 2.0 | 1.3 |

11a) because of the more frequent occurrence of intense rain rates in the *RHB* dataset. This is especially true in EPIC for the sub-MCS category (Fig. 11c). The difference in the heavy rain portion of the distributions is most likely due to the difference in spatial resolution of the PR and *RHB* datasets (see section 2).

In the PR climatology, the EPIC probability distributions are shifted slightly to the right (i.e., higher rain rates) of the corresponding TEPPS distributions for all feature categories except NCs. There is generally a higher probability of rain rate above ~3 mm h$^{-1}$ in both the sub-MCS (Fig. 11c) and MCS (Fig. 11b) categories. The net result is to produce higher mean and median rain rates in the EPIC region. The higher rain rates in the sub-MCS and MCS categories are consistent with the higher echo tops and higher reflectivity structure observed by the PR in the EPIC region (Figs. 5, 7). The rain-rate distributions in the NC category are nearly identical in both the PR and *RHB* datasets. As expected, these features generally produce very low rain intensities.

As noted in section 2, the PR rain rates in this study are calculated using Eq. (1). Because Eq. (1) was derived using in situ data collected during EPIC, it is of interest to compare the PR rain-rate results using the standard TRMM 2A25 product. As described in Iguchi et al. (2000), when the surface reference technique is deemed reliable, the *Z–R* in each vertical profile of the PR 2A25 rainfall product is adjusted from an initial DSD to match the profile's attenuation characteristics. This adjustment occurs preferentially in heavy rain where significant attenuation is present in the profile. The difference in PR rain-rate distributions using the different *Z–R* relations is shown in Fig. 12. The result of applying the *Z–R* relation in the 2A25 product is to increase the occurrence of rain rates above about 2–3 mm h$^{-1}$ in the TEPPS and EPIC PR dataset and to increase the mean rain rates by about 25% (not shown). Although the application of the 2A25 rain rates to the PR data does not change the overall study results, it does provide an indication of the uncertainty in the rainfall calculations used in this study.

The field campaign rain-rate results show many similarities with respect to the PR climatology for the two regions (Fig. 11). Similar to the PR, the EPIC *RHB* rain rates have a higher probability of occurrence of intense rain rates for sub-MCSs and MCSs. The more frequent rain rates above 4 mm h$^{-1}$ are responsible for the larger EPIC mean rain rate compared with TEPPS (Table 4). These relatively heavy rain rates are due to a combination of moderate–large-sized sub-MCS (100–1000 km$^2$) and MCS features (Fig. 13). EPIC *RHB* features also have a more frequent occurrence of light rain rates (below the detection of the PR) compared with TEPPS. The lower rain rates result in a lower EPIC median value (50% cumulative frequency). These differences in light rain occurrence are especially pronounced in the sub-MCS and NC categories (Figs.

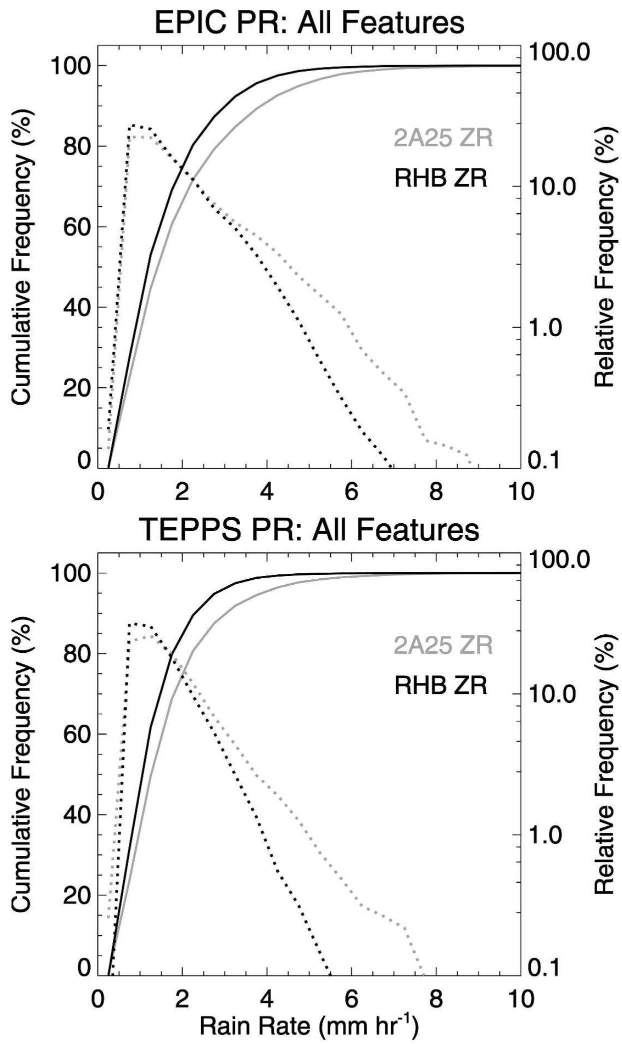


FIG. 12. Comparison of TRMM PR conditional rain-rate distributions using the *Z–R* in Eq. (1) and the 2A25 *Z–R* relation for the (top) EPIC and (bottom) TEPPS regions. Cumulative (relative) frequency histograms are indicated by the solid (dashed lines). The Eq. (1) and 2A25 distributions are indicated by the black and gray lines, respectively.

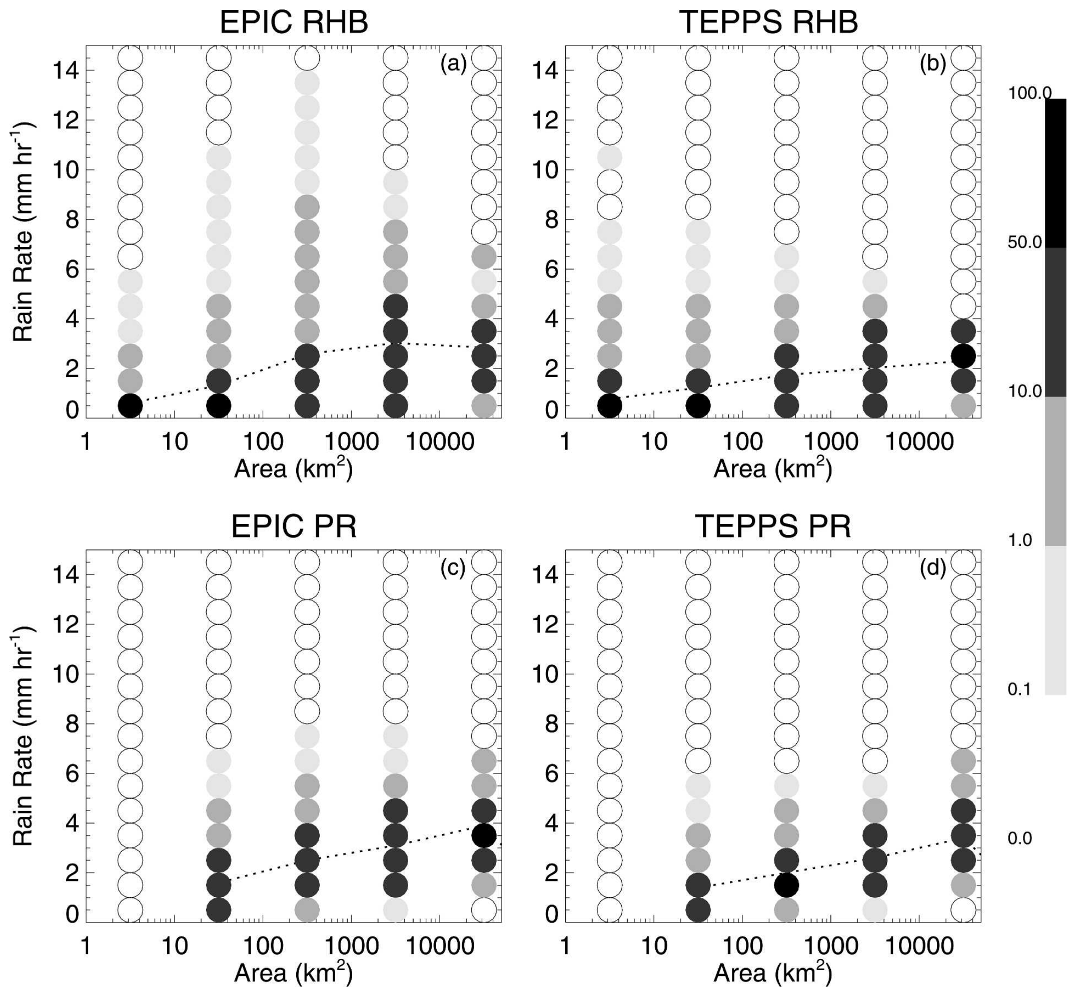


FIG. 13. Feature mean conditional rain rate as a function of area for (a) EPIC *RHB*, (b) TEPPS *RHB*, (c) EPIC PR, and (d) TEPPS PR data. Relative frequency (%) of rain-rate occurrence is indicated by the circle shading, according to the legend at the rhs of the figure. The dotted line in (a)–(d) represents the mean of the distribution.

11c,d) and are associated with the smallest features (<50 km$^2$) sampled by the *RHB* (Fig. 13). The greater frequency of EPIC *RHB* rain rates below 1 mm h$^{-1}$ is consistent with the increased frequency of small, low clouds (i.e., precipitating trade wind cumulus) that were more prevalent during the EPIC field campaign. In the MCS category (Fig. 11b), there is little difference in the EPIC and TEPPS light rain frequency of occurrence; however, similar to the sub-MCS category, the *RHB* EPIC histogram shows a higher probability of rain rates above about 4 mm h$^{-1}$. The fact that EPIC MCSs and sub-MCSs have a higher frequency of intense rain rates is consistent with the reflectivity distributions shifted to higher reflectivity values above the freezing level in these features (Figs. 9, 10).

To more effectively compare the *RHB* and PR rain rates, sensitivity tests were performed using a 20-dB*Z* feature threshold in the *RHB* dataset (i.e., the same threshold as used in the PR dataset). As expected, raising the *RHB* feature threshold from 10 to 20 dB*Z* increases the mean *RHB* rain rates in Table 4 (approximately 50% for the all-feature category) and shifts the *RHB* rain-rate distributions to the right in Fig. 11. The biggest effect is on sub-MCS and NC rain rates. However, changing the *RHB* minimum feature threshold does not change the relative differences between EPIC and TEPPS and has little other effect on the rainfall characteristics discussed in this study.

Given the previously discussed differences in rain intensity and echo-top heights, it is of interest to compare the rain volume contribution as a function of feature vertical structure. Figure 14 shows the distribution of volumetric rainfall as a function of mean maximum 20-dB*Z* echo height for the different feature categories. The relative contribution of the MCS, sub-MCS, and NC categories to the total rainfall volume (i.e., the in-

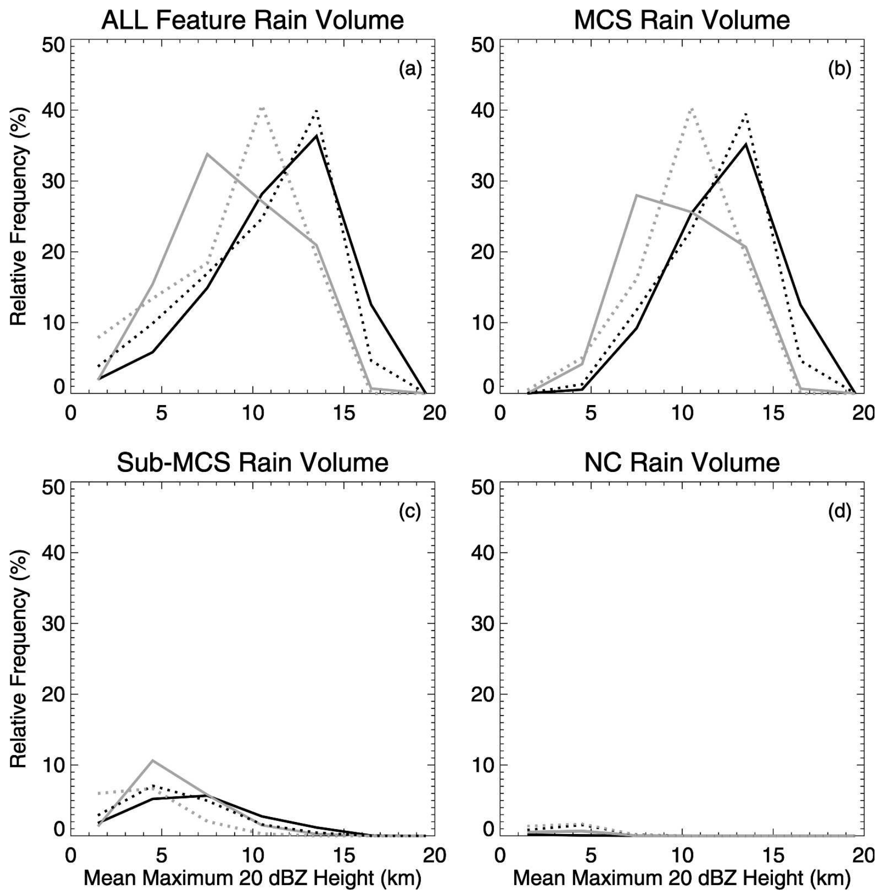


FIG. 14. Relative frequency of rainfall volume as a function of feature maximum 20-dB$Z$ height for (a) all, (b) MCS, (c) sub-MCS, and (d) NC feature categories. Solid black (gray) lines represent EPIC (TEPPS) *RHB* data. Dashed black (gray) lines represent EPIC (TEPPS) TRMM PR data.

tegrated sum under the curves in Figs. 14b–d) is shown in Table 5.

The most salient feature of Fig. 14 is that the vast majority of volumetric rain in the EPIC and TEPPS regions is contributed by MCSs. In both the PR and *RHB* observations, MCSs provide 79%–83% of the total rainfall volume (Table 5). These percentages are similar to previous results from the west Pacific TOGA COARE region (Rickenbach and Rutledge 1998) as well as to the eastern Atlantic during the Global Atmospheric Research Programme Atlantic Tropical Experiment (López 1978). In the EPIC region, the maximum MCS contribution is associated with a sharp peak in the echo-top distribution at 13.5 km in both the TRMM climatology and the field campaign datasets (Fig. 14b), indicating that relatively deep MCSs produce the bulk of the rainfall volume. In contrast, the TEPPS MCS distribution is wider, with significant rain volume contributions from shallower echo tops. The contribution of relatively shallow systems to total rainfall is consistent with Berg et al. (2002), who examined precipitation characteristics in portions of the west and east Pacific (including the TEPPS region) using satellite data. The contribution from shallower MCSs is especially pronounced during the TEPPS field campaign. In this case, the TEPPS distribution shows significant rain volume contributions from echo tops ranging from 7.5 to 13.5 km. Similar differences in EPIC and TEPPS rainfall contributions are also observed in the sub-MCS category (Fig. 14c); the EPIC contribution is shifted to the right (higher echo tops) relative to TEPPS in both the PR and *RHB* datasets. As anticipated, NCs

TABLE 5. Rain volume fraction by feature category.

| | MCS (%) | Sub-MCS (%) | NC (%) |
|---|---|---|---|
| EPIC *RHB* | 82.8 | 16.8 | 0.4 |
| EPIC PR | 80.2 | 17.2 | 2.6 |
| TEPPS *RHB* | 79.0 | 19.6 | 1.4 |
| TEPPS PR | 81.4 | 15.3 | 3.3 |

have a negligible contribution to the rainfall volume (Fig. 14d).

Combining the individual feature categories (Fig. 14a), the volumetric rain in the TEPPS region reflects an overlapping contribution by sub-MCSs and MCSs in the 4.5–13.5-km height range as well as deep MCSs while the EPIC rainfall is dominated by deep MCSs only. As noted above, the shallow MCS contribution is especially pronounced during the TEPPS field campaign.

## 4. Summary and conclusions

This paper compares the horizontal and vertical structure of precipitation features in two regions of the east Pacific where recent field campaigns (i.e., EPIC and TEPPS) have been conducted. Precipitation features are objectively identified in both field campaign ship-based and TRMM PR (1998–2004) radar data and the resulting statistics are compared among the datasets.

EPIC MCSs and sub-MCSs larger than 100 km$^2$ were found to be deeper, had larger reflectivities extending above the freezing level, and had higher rain rates compared with TEPPS. Similar to results from previous studies, MCSs provided the vast majority of total rainfall even though they occurred only 3%–5% of the time. In terms of smaller features, there were several important differences between the PR and field campaign datasets. During the EPIC campaign, there was an abundance of small (<100 km$^2$), shallow clouds (trade wind layer) that reduced the overall size and height distributions of these features relative to the TRMM climatology for the EPIC region. These features produced very light rain rates. The prevalence of small, low echo-top features in the EPIC ship dataset was probably a consequence of periodic dry air intrusions that were documented with upper air sounding data during the campaign. Previous studies have shown that both the Costa Rica thermocline dome and the equatorial cold tongue were source regions for dry air during the EPIC experiment (Xie et al. 2005; Zuidema et al. 2006). Despite the occurrence of dry air intrusions during the EPIC campaign, the mean rain rates were higher compared with TEPPS for all feature categories except NCs.

In the TEPPS region, the ship data showed that sub-MCSs were deeper and larger compared with the TRMM satellite climatology. The change may have been associated with the 1997/98 El Niño that produced higher than normal SSTs across the central and eastern Pacific. Both the satellite and ship data showed that the EPIC region contained a higher rainfall fraction of convective precipitation compared with TEPPS and that ice processes contributed more to rainfall production in the EPIC region compared with the TEPPS region.

We note that the 7-yr TRMM PR data used in this study do exhibit significant interannual and intraseasonal variability. In particular, the 2002/03 El Niño event was observed in the TEPPS statistics as an increase in mean feature rain area and rain volume properties. The statistics in the EPIC region included the passage of five tropical cyclones, which were reflected as similar increases in feature statistics (e.g., feature area and mean maximum 20-dB*Z* echo height). Although El Niño and tropical cyclone activity changed the magnitude of the statistical parameters examined, the relative differences between the EPIC and TEPPS regions were consistent with the 7-yr climatology results discussed in section 3, indicating that the differences between EPIC and TEPPS reported herein are robust.

As mentioned in the introduction, the variability in convective characteristics across the tropical Pacific has important implications for satellite algorithms designed to retrieve surface rainfall and latent heating characteristics from passive microwave signatures. Although this study does not resolve the issue of TRMM rainfall discrepancies in the east Pacific, it does highlight differences in hydrometeor vertical structure between the EPIC and TEPPS regions, which must be properly understood for improvements in satellite-based rainfall retrievals. Future work will be directed at analyzing the diurnal cycle of precipitation features and extending the analysis technique to other regions where field campaigns have been conducted.

*Acknowledgments.* The authors thank Ed Zipser, Paquita Zuidema, and one anonymous reviewer for their constructive comments, which improved the manuscript. Bob Houze and Jasmine Cetrone also provided helpful suggestions on this work. Dave Wolff at the NASA TRMM Office provided the QC algorithm for the EPIC and TEPPS ship radar data. The authors extend their appreciation to all of the people who helped collect data during the EPIC and TEPPS field campaigns. This work was supported by NSF Grants ATM-0002256 and ATM-0340544 and NASA PMM Grant NAG5-13623.

REFERENCES

Berg, W., C. Kummerow, and C. A. Morales, 2002: Differences between east and west Pacific rainfall systems. *J. Climate,* **15,** 3659–3672.

Cetrone, J., and R. A. Houze Jr., 2006: Characteristics of tropical convection over the ocean near Kwajalein. *Mon. Wea. Rev.,* **134,** 834–853.

Cheng, C.-P., and R. A. Houze Jr., 1979: The distribution of convective and mesoscale precipitation in GATE radar echo patterns. *Mon. Wea. Rev.,* **107,** 1370–1381.

Cifelli, R., S. A. Rutledge, D. J. Boccippio, and T. Matejka, 1996: Horizontal divergence and vertical velocity retrievals from Doppler radar and wind profiler observations in tropical convection. *J. Atmos. Oceanic Technol.,* **13,** 948–966.

DeMott, C. A., and S. A. Rutledge, 1998: The vertical structure of TOGA COARE convection. Part I: Radar echo distributions. *J. Atmos. Sci.,* **55,** 2730–2747.

Houze, R. A., Jr., 1993: *Cloud Dynamics.* Academic Press, 573 pp.

——, and C.-P. Cheng, 1977: Radar characteristics of tropical convection observed during GATE: Mean properties and trends over the summer season. *Mon. Wea. Rev.,* **105,** 964–980.

Iguchi, T., and R. Meneghini, 1994: Intercomparison of single-frequency methods for retrieving a vertical rain profile from airborne or spaceborne radar data. *J. Atmos. Oceanic Technol.,* **11,** 1507–1516.

——, T. Kozu, R. Meneghini, J. Awaka, and K. Okamoto, 2000: Rain-profiling algorithm for the TRMM precipitation radar. *J. Appl. Meteor.,* **39,** 2038–2052.

Janowiak, J. E., P. A. Arkin, P. Xie, M. L. Morrissey, and D. R. Legates, 1995: An examination of the east Pacific ITCZ rainfall distribution. *J. Climate,* **8,** 2810–2823.

Johnson, R. H., T. M. Rickenbach, S. A. Rutledge, P. E. Ciesielski, and W. H. Schubert, 1999: Trimodal characteristics of tropical convection. *J. Climate,* **12,** 2397–2418.

Kummerow, C., W. Barnes, T. Kozu, J. Shiue, and J. Simpson, 1998: The Tropical Rainfall Measuring Mission (TRMM) sensor package. *J. Atmos. Oceanic Technol.,* **15,** 809–817.

Loehrer, S. M., T. A. Edmands, and J. A. Moore, 1996: TOGA COARE upper-air sounding data archive: Development and quality control procedures. *Bull. Amer. Meteor. Soc.,* **77,** 2651–2671.

López, R. E., 1977: The lognormal distribution and cumulus cloud populations. *Mon. Wea. Rev.,* **105,** 865–872.

——, 1978: Internal structure and development processes of C-Scale aggregates of cumulus clouds. *Mon. Wea. Rev.,* **106,** 1488–1494.

Mapes, B. E., and J. Lin, 2005: Doppler radar observations of mesoscale wind divergence in regions of tropical convection. *Mon. Wea. Rev.,* **133,** 1808–1824.

——, T. T. Warner, M. Xu, and A. J. Negri, 2003: Diurnal patterns of rainfall in northwestern South America. Part I: Observations and context. *Mon. Wea. Rev.,* **131,** 799–812.

Mechoso, C. R., and Coauthors, 1995: The seasonal cycle over the tropical Pacific in coupled ocean–atmosphere general circulation models. *Mon. Wea. Rev.,* **123,** 2825–2838.

Mohr, C. G., L. J. Miller, R. L. Vaughan, and H. W. Frank, 1986: The merger of mesoscale datasets into a common Cartesian format for efficient and systematic analyses. *J. Atmos. Oceanic Technol.,* **3,** 143–161.

Molinari, J., D. Vollaro, S. Skubis, and M. Dickenson, 2000: Origins and mechanisms of eastern Pacific tropical cyclogenesis: A case study. *Mon. Wea. Rev.,* **128,** 125–139.

Nesbitt, S. W., E. J. Zipser, and D. J. Cecil, 2000: A census of precipitation features in the Tropics using TRMM: Radar, ice scattering, and lightning observations. *J. Climate,* **13,** 4087–4106.

——, R. Cifelli, and S. A. Rutledge, 2006: Storm morphology and rainfall characteristics of TRMM precipitation features. *Mon. Wea. Rev.,* **134,** 2702–2721.

Newell, R. E., J. W. Kidson, D. G. Vincent, and G. J. Boer, 1974: *The General Circulation of the Tropical Atmosphere*. Vol. 2. MIT Press, 371 pp.

Patterson, V. L., M. D. Hudlow, P. J. Pytlowaney, F. P. Richards, and J. D. Hoff, 1979: GATE radar rainfall processing system. NOAA Tech. Memo. EDIS 26, Washington, DC, 34 pp. [Available from the National Technical Information Service, Sills Building, 5285 Port Royal Rd., Springfield, VA 22161.]

Petersen, W. A., R. Cifelli, D. J. Boccippio, S. A. Rutledge, and C. Fairall, 2003: Convection and easterly wave structure in the eastern Pacific warm pool during EPIC-2001. *J. Atmos. Sci.,* **60,** 1754–1773.

——, H. J. Christian, and S. A. Rutledge, 2005: TRMM observations of the global relationship between ice water content and lightning. *Geophys. Res. Lett.,* **32,** L14189, doi:10.1029/2005GL023236.

Raymond, D. J., G. B. Raga, C. S. Bretherton, J. Molinari, C. López-Carillo, and Z. Fuchs, 2003: Convective forcing in the intertropical convergence zone east Pacific. *J. Atmos. Sci.,* **60,** 2064–2082.

——, and Coauthors, 2004: EPIC2001 and the coupled ocean–atmosphere system of the tropical east Pacific. *Bull. Amer. Meteor. Soc.,* **85,** 1341–1354.

Rickenbach, T. M., and S. A. Rutledge, 1998: Convection in TOGA COARE: Horizontal scale, morphology, and rainfall production. *J. Atmos. Sci.,* **55,** 2715–2729.

Serra, Y. L., and R. A. Houze Jr., 2002: Observations of variability on synoptic timescales in the east Pacific ITCZ. *J. Atmos. Sci.,* **59,** 1723–1743.

Short, D. A., and K. Nakamura, 2000: TRMM radar observations of shallow precipitation over the tropical oceans. *J. Climate,* **13,** 4107–4124.

——, P. A. Kucera, B. S. Ferrier, J. C. Gerlach, S. A. Rutledge, and O. W. Thiele, 1997: Shipboard radar rainfall patterns within the TOGA COARE IFA. *Bull. Amer. Meteor. Soc.,* **78,** 2817–2836.

Steiner, M., R. A. Houze Jr., and S. E. Yuter, 1995: Climatological characteristics of three-dimensional storm structure from operational radar and raingauge data. *J. Appl. Meteor.,* **34,** 1978–2007.

Sui, C.-H., K.-M. Lau, Y. N. Takayabu, and D. A. Short, 1997: Diurnal variations in tropical oceanic cumulus convection during TOGA COARE. *J. Atmos. Sci.,* **54,** 639–655.

Vincent, D. G., and A. H. Fink, 2001: Tropical cyclone environments over the northeastern and northwestern Pacific based on ERA-15 analyses. *Mon. Wea. Rev.,* **129,** 1928–1948.

Wang, C., and D. B. Enfield, 2001: The tropical western hemisphere warm pool. *Geophys. Res. Lett.,* **28,** 1635–1638.

——, and ——, 2003: A further study of the tropical Western Hemisphere warm pool. *J. Climate,* **16,** 1476–1493.

Xie, P., and P. A. Arkin, 1996: Analyses of global monthly precipitation using gauge observations, satellite estimates, and numerical model predictions. *J. Climate,* **9,** 840–858.

Xie, S.-P., H. Xu, W. S. Kessler, and M. Nonaka, 2005: Air–sea interaction over the eastern Pacific warm pool: Gap winds, thermocline dome, and atmospheric convection. *J. Climate,* **18,** 5–20.

Yuter, S. E., and R. A. Houze Jr., 1995: Three-dimensional kinematic and microphysical evolution of Florida cumulonimbus. Part II: Frequency distributions of vertical velocity, reflectivity, and differential reflectivity. *Mon. Wea. Rev.,* **123,** 1941–1963.

——, and ——, 2000: The 1997 Pan American Climate Studies Tropical Eastern Pacific Process Study. Part I: ITCZ region. *Bull. Amer. Meteor. Soc.,* **81,** 451–481.

Zuidema, P., B. Mapes, J. Lin, C. Fairall, and G. Wick, 2006: The interaction of clouds and dry air in the eastern tropical Pacific. *J. Climate,* **19,** 4531–4544.